Article

Journal of
Nanoscience and Nanotechnology
Vol. 20, 7333–7341, 2020
www.aspbs.com/jnn

Synthesis of Novel Pd Nanosponges for Non-Enzymatic Glucose Sensor

Feng Chen[1], Jing-Hao Li[1], Yu-Chen Chi[1], Zhen-Hua Dan[2], and Feng-Xiang Qin[1,*]

[1] School of Materials Science and Engineering, Nanjing University of Science and Technology, Nanjing 210094, China
[2] College of Materials Science and Engineering, Nanjing TECH University, Nanjing 210009, China

A unique nanostructured electrocatalyst based on Palladium (Pd) nanosponge architecture is synthesized by one-step dealloying of the amorphous alloy precursor with low Pd concentration. The sponge-like nanostructure with hollow interiors enables sufficient contact between reactants and both the interior and exterior surfaces. The results of cyclic voltammetry reveal that the as-prepared Pd nanosponge exhibits high sensitivity of 32 μA mM^{-1} cm^{-2} in a wide linear range (1–18 mM), and long-term stability toward glucose electro-oxidation. The Pd nanosponge also manifests detection limit as low as 2.0 μM ($S/N = 3$) and high selectivity for glucose sensing. The enhanced catalytic activity of the Pd nanosponge is attributed to the bimetallic synergistic effect and the large active surface area of the high-uniformity porous structure. The facile synthesis of the cost-effective Pd nanosponge with superior electrocatalytic performance makes it hold great potentials for biosensor and other catalysis applications.

Keywords: Amorphous Alloy, Dealloying, Pd Nanosponge, Electrocatalysis.

1. INTRODUCTION

Recently, the nanostructed materials have attract increasing interests, due to their utilizing potentials in catalysis, chemical sensors and biotechnology fields [1–8]. Especially, the nanoporous metals, with three-dimensional bicontinuous microstructure and large surface areas, enable the full exposure of active surface to the electrolyte and provide a short transportation path for electrons and ions, leading to faster reaction kinetics and higher electrocatalytic reactivity [9, 10]. Dealloying is one of effective methods to fabricate nanoporous metals which is the selective dissolution of one or more of the elemental components of an alloy [1, 11]. During the dealloying process, more chemically active atoms are dissolved in a precursor alloy which is composed of more than two different elements [2, 12]. Mean while, surface diffusion and aggregation of chemically inert atoms result in the formation of a nanoporous structure with nanoscale pores and ligaments [13]. Amorphous alloys with a monolithic phase is believed to be optimization since they are precursors beneficial to forming a uniform nanoporosity upon simple dealloying treatment owing to the absence of the intermetallic phases, grain boundaries and phase segregation.

So far, various nanoporous metals or their oxides/hydroxides have been prepared from amorphous alloy precursors [14, 15]. Nanoporous Pd and its alloys exhibit outstanding sensing performance towards the detection of hydrogen peroxide and glucose [16]. Nanoporous Pd with a bicontinuous network structure is proved to have high catalytic activity, good stability and selectivity towards the oxidation of glucose with a relatively lower cost [17].

Although much attention has been paid to the fabrication of nanoporous Pd [18–21], most of these researches involved the complicated processes, the employment of organic reagents, or utilization of the alloys with high Pd concentration. Therefore, it is highly desirable to synthesize nanoporous Pd with high catalytic performance using a simple preparation method from low Pd-loading alloys.

In this research, a unique nanostructured electrocatalyst based on Pd nanosponge (Pd NS) was synthesized by one-step dealloying of a $Ti_{40}Zr_{10}Cu_{36}Pd_{14}$ amorphous alloy. The amorphous precursor was chosen instead of crystalline alloy, because of the chemical and structural homogeneity of amorphous alloy without crystallographic defects, which is beneficial to the formation of fine and uniform pores [22]. Besides, the $Ti_{40}Zr_{10}Cu_{36}Pd_{14}$ amorphous alloy with low Pd concentration may further reduce the cost of the catalysts. The electrocatalytic performances of the

*Author to whom correspondence should be addressed.

unique Pd nanosponge were investigated in concentrated KOH solution with the addition of glucose.

2. EXPERIMENTAL DETAILS

The mother alloy with nominal atomic composition of $Ti_{40}Zr_{10}Cu_{36}Pd_{14}$ was prepared by arc melting the mixture of pure metals (>99.9 mass%) in an argon atmosphere. $Ti_{40}Zr_{10}Cu_{36}Pd_{14}$ ribbons with 5 mm in width and 70 μm in thickness were prepared by a melt spinning method. The ribbon samples were dealloyed under a current density of 10 mA cm^{-2} in 1.0 M $(NH_4)_2SO_4$ + 0.5 wt% NH_4F solution at room temperature for different times (5, 20 and 40 mins). Surface morphologies of dealloyed samples were observed by scanning electron microscopy (SEM) equipped with X-ray energy dispersive spectroscopy (EDS). The microstructures of the dealloyed samples were investigated by high resolution transmission electron microscopy (HRTEM, JEOL 2010). In order to analyze elemental information, X-ray photoelectron spectroscopy (XPS) of the dealloyed samples were measured by means of Shimadzu Kratos produced AXIS-ultra DLD photoelectron spectrometer with monochromatized Al Kαexcitation (hγ = 1486.6 eV). XPS depth profile was conducted at an etching rate of 13.3 nm min^{-1} corresponding to the rate in silicon dioxide.

To investigate the electrochemical catalytic performances of the Pd NS, electrochemical experiments were carried out using a PARSTAT 4000 workstation at room temperature. A conventional three-electrode cell with a Pt plate electrode as a counter electrode, a saturated calomel electrode (SCE) as a reference electrode, and the samples as the working electrode was used. The preparation process of the Pd NS working electrode was described below: 6 mg fine ground dealloyed samples, 120 μL ethanol, and 30 μL Nafion solution (0.5 wt%) were ultrasonically mixed. Then, 10 μL of the homogeneously mixed catalyst solution was placed on a freshly polished glassy carbon (GC) electrode with a diameter of 5 mm. The cyclic voltammetry curves of Pd NS were obtained in 1.0 M KOH + 50 mM glucose solution with the scan rate of 50 mV s^{-1}.

3. RESULTS AND DISCUSSION

3.1. Microstructural Characterization of Pd NS

The microstructure of the $Ti_{40}Zr_{10}Cu_{36}Pd_{14}$ amorphous alloy before dealloying is investigated, with only a halo peak in the XRD pattern (not shown) indicating that a glassy phase is formed in the as-spun ribbons. Figure 1 demonstrates the surface morphologies of $Ti_{40}Zr_{10}Cu_{36}Pd_{14}$ amorphous alloy after dealloying in 1.0 M $(NH_4)_2SO_4$ + 0.5 wt% NH_4F solution for different times (5, 20 and 40 mins). Before dealloying, the surface of $Ti_{40}Zr_{10}Cu_{36}Pd_{14}$ amorphous alloy is a typical featureless structure (not shown). It's found that the morphology

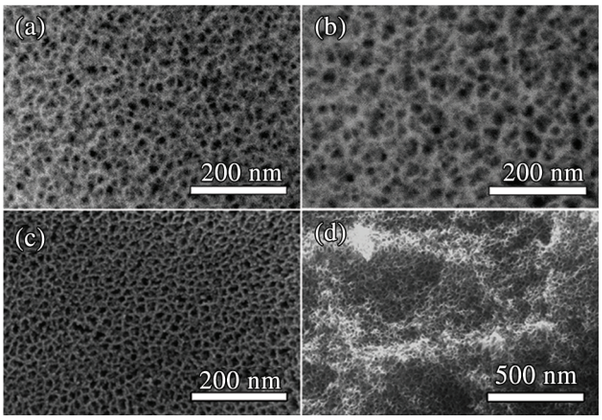

Figure 1. Top-view surface SEM images of $Ti_{40}Zr_{10}Cu_{36}Pd_{14}$ amorphous alloy after dealloying for 5 mins (a), 20 mins (b), 40 mins (c) and SEM image of the internal part of 40-min dealloyed sample (d).

of the surface strongly depends on the dealloying duration, although the nanoporous structures are formed on all samples by dealloying for 5, 20 and 40 mins. For the samples dealloyed for 5 and 20 mins, some undeveloped and disordered pores with mean diameters of 11.2 nm and 14.3 nm respectively are observed in the surface, as evidenced by the top-view surface SEM images (Figs. 1(a) and (b)). With the increase of dealloying time up to 40 mins, a well-developed and ordered nanoporous and network structure with mean pore diameter of about 15.5 nm, is formed on the surface of $Ti_{40}Zr_{10}Cu_{36}Pd_{14}$ amorphous alloy as exhibited in Figure 1(c). It should be noted that a bicontinuous sponge-like structure with specific orientations pore channels is observed in the interior of the sample after dealloying for 40 mins, as presented in Figure 1(d), indicating that the sample is fully dealloyed.

The microstructures of the dealloyed samples were further investigated by means of TEM. Figure 2 displays the bright-field TEM, high-resolution TEM images and corresponding SAD patterns of the amorphous alloy dealloyed for different times. Figures 2(a)–(c) demonstrate the corresponding typical TEM images of the dealloyed samples for different times, where the nanoporous microstructure with average ligament size of ~5.1 nm is exhibited. As shown in the insets of Figures 2(a)–(c), several ring patterns appearing in the corresponding SAD pattern are identified as a cubic Pd phase in nanoscale with crystal planes of (111), (200), (220), (222) and (420). Moreover, the existence of a Cu_3Pd phase is confirmed by high-resolution TEM of local marked area in the 5-min dealloyed sample in Figure 2(a), suggesting that some Cu element retains in the connecting ligaments of the nanoporous structure in the initial period of dealloying. HRTEM images (Figs. 2(d) and (e)) provide that the ordered lattice fringes are well resolved with the lattice spacing calculated to be 3.40 Å and 3.56 Å corresponding to the (103) and (102) crystal plane of Cu_3Pd phase (Fig. 2(d)), and 2.24 Å corresponding to the (113) crystal plane of cubic Pd phase (Fig. 2(e)).

The ligaments are found to be comprised of nanocrystals with a grain size of ∼5 nm. The tends of pore size and ligament size vs dealloying time in Figure 2(f) indicate the decreasing of the ligaments accompanied with the increasing of the pore size.

To further analyze the chemical information of the as-prepared Pd NS, more detailed elemental information of the dealloyed layer was analyzed by XPS. As illustrated in Figure 3(a), XPS spectra of as-prepared surface over a wide binding energy region exhibit peaks of C, O, Zr, Ti, Pd and Cu. O1 s peak is overlapped with that of Pd 3*p*3/2. Therefore, in this case, the concentration of O is identified by O KLL peak. After dealloying for 40 mins, strong peaks of Pd 3*d*, Pd 3*p* and Pd MNN with small signal of Cu 2*p* are mainly detected. The XPS elemental depth profile was also carried out, the results can be observed in Figure 3(b). Atomic concentration of Pd is about 80% in the surface of the sample after dealloying, which decreases to 20% in the depth of 1600 nm from the top surface of the sample.

Figure 4 shows the 3D waterfall graphs of XPS spectra of Ti 2*p* (a), Zr 3*d* (b), Cu 2*p* (c) and Pd 3*d* (d) as sputtering depth increasing. As presented in Figures 4(a) and (b), the peaks of Ti 2*p* at 460.0 eV and 453.8 eV and Zr 3*d* at 181.2 eV and 178.8 eV can't be detected until the sputtering depth increases up to 1200 nm of the 40-min dealloyed sample, suggesting that Ti and Zr are fully dealloyed in the considerable thickness. Moreover, a small amount of Cu constituents in metallic state still exists in the top surface, as shown in Figure 4(c). When the sputtering depth is 2 nm under the initial surface after sputtering for 15 s, Pd 3*d* peaks are located at 340.4 eV and 335.2 eV, originating from Pd metal in metallic state. Moreover, as it is noticed that the binding energies of Pd 3*d* are shifted to higher values (342.6 and 337.2 eV) which are assigned to PdO and PdO_2 in the most top surface, as illustrated in Figure 4(d). Here, the existence of PdO and PdO_2 existing in the most top surface is believed to result from the strong oxygen adsorption on NP Pd during the polarization at high anodic potentials. The results of the XPS characterization are correspondent with the results of TEM and the formation mechanization of Pd NS.

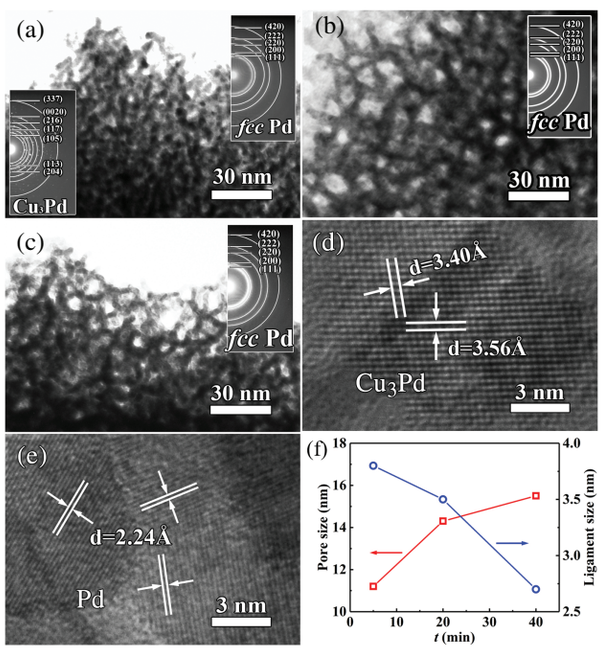

Figure 2. BF-TEM images and the corresponding SAD patterns of the amorphous alloy after dealloying for 5 mins (a), 20 mins (b), 40 mins (c) and HR-TEM images of the 40-min dealloyed sample (d, e), the proe size and ligament size versus the dealloying time (f).

3.2. Electrocatalytic Performance of Pd NS

Figure 5(a) displays the cyclic voltammetry (CV) curves of the Pd NS electrode in 1.0 M KOH solution with the scan rate of 50 mV s^{-1}. The CV curves of pure Pd plate are also presented for the comparison. The appearance of the oxidation peak from −0.35 to 0.10 V indicates that the surface Pd is oxidized to be Pd oxides in the forward scan, and then the reduction reaction takes place at about −0.41 V to form metallic Pd in the backward scan. The oxidation and reduction current densities of Pd NS are much higher than those of Pd plate, which is mainly attributed to the large amount of electrochemical active sites of Pd NS with large surface area.

The electrocatalytic performances on the glucose oxidation of the Pd NS were also examined to evaluate its potential application as glucose detector. Figure 5(b) illustrates the CV curves of the Pd NS and Pd plate in 1.0 M KOH+ 50 mM glucose solution with the scan rate of 50 mV s^{-1}. The electro-oxidation of glucose is characterized by two well-defined anodic peaks on the forward and backward scans. The first peak located at −0.68 V results from the electrochemical adsorption of glucose, which generates the initial oxidation current. With the electrochemical reaction going on, the accumulation of the absorbed intermediates produced by dehydrogenation on the Pd NS surface blocks the further electro-absorption of glucose, bringing about the decrease of current density [23]. As the potential gradually increases, Pd-OH species are generated in the alkaline solution, which are beneficial for the oxidation of intermediates on the catalyst surface [24]. The second oxidation peak located at −0.2 V, corresponds to the complete oxidation of glucose after the poisoning intermediates on the electrocatalyst surface are moved by the OH_{ads} radicals formed by the partial discharge of OH^- under the upper potential region [25].

In the forward scan, the peak potential and peak current density are −0.26 V and 3.1 mA cm^{-2} for the Pd plate electrode, −0.20 V and 14.0 mA cm^{-2} for the Pd NS electrode (Table I). In the backward scan, they are −0.41 V and 2.6 mA cm^{-2} for the Pd plate one and −0.41 V and −6.1 mA cm^{-2} for the Pd NS. The peak current density for the Pd NS is over 4 times higher than that for Pd

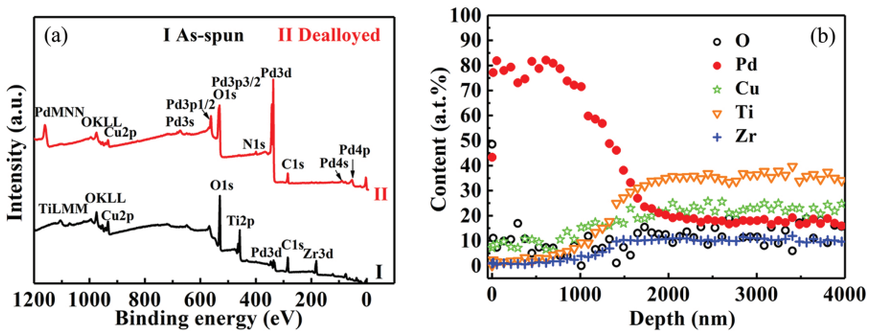

Figure 3. XPS spectra of the surfaces before and after dealloying for 40 mins (a) and XPS elemental depth profile (b).

plate. The onset potential (E_{onset}) for the glucose oxidation on Pd NS electrode is 90 mV lower than that on the Pd plate electrode. The significantly negative shift of the E_{onset} and the higher peak current density for the glucose electro-oxidation on the Pd NS electrode reveal that the more favorable reaction kinetics for glucose oxidation on the Pd NS electrode, which results in superior electrocatalytic activity towards glucose electro-oxidation in alkaline media. In addition, the value of j_F/j_B, which is the ratio of the forward and backward anodic peak current densities, is 2.3 for Pd NS electrode, and that for Pd plate electrode is 1.2. The higher j_F/j_B value of Pd NS implies that more glucose are oxidized in the forward scan, suggesting the excellent poisoning tolerance of the Pd NS to carbonaceous oxidative intermediates [26].

The electrochemical stability of the Pd NS electrode was investigated by CV tests for 100 potential cycles performed in 1.0 M KOH+50 mM glucose solution, as shown in Figure 5(c). No obvious change can be found in the potential and current density of the oxidation peak after 10 cycles. After 100 cycles, the current density of the oxidation peak decreases 16%, hinting the high stability of the catalytic performance of Pd NS.

For demonstration of the improved glucose sensing and continuous monitoring performance of the Pd NS, the sensitivity, linear range and detection limit of Pd NS are evaluated by amperometry method. Figure 6(a) presents the amperometric current response of the Pd NS at −0.25 V in 0.1 M KOH stirred at 150 rpm. Upon successive addition of 1 mM glucose at a regular interval time of 60 s,

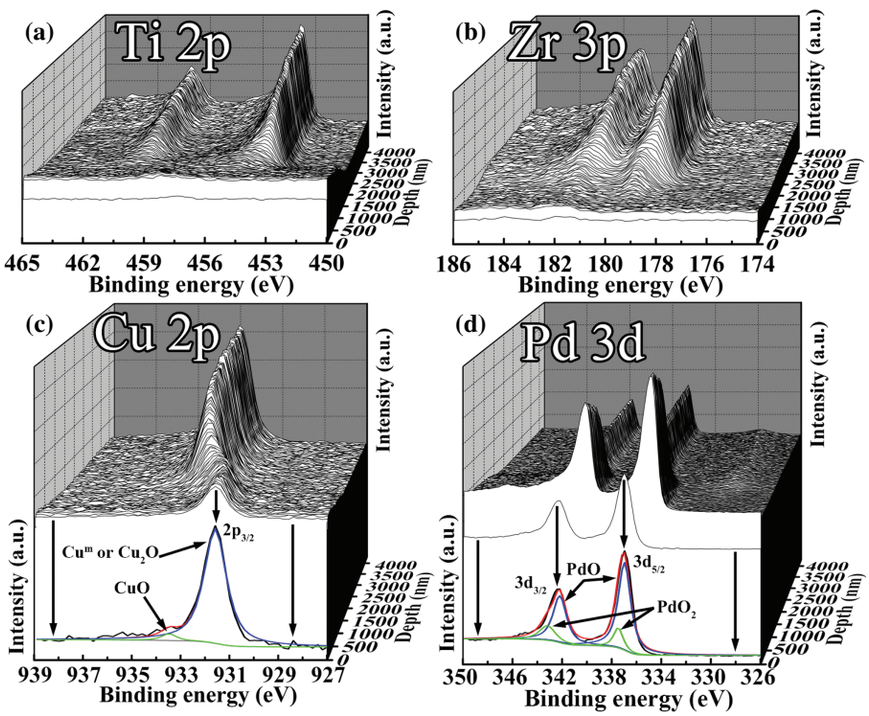

Figure 4. 3D waterfall graphs of the XPS spectra of Ti 2*p* (a), Zr 3*d* (b), Cu 2*p* (c) and Pd 3*d* (d) with different sputtering depth.

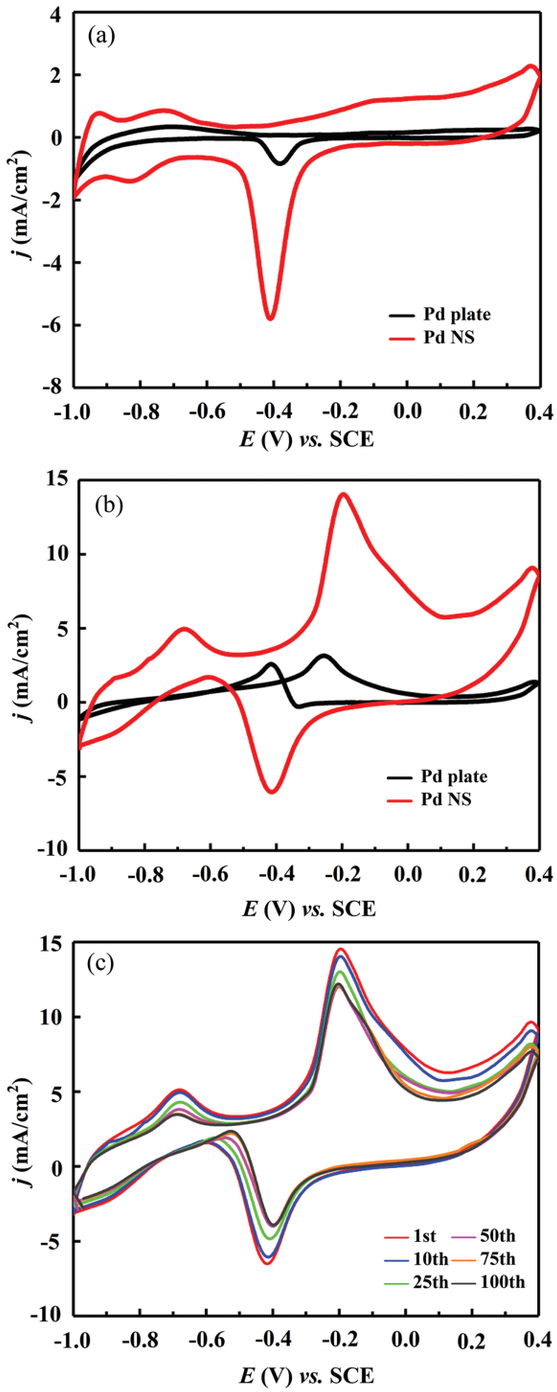

Figure 5. CV curves of Pd plate and Pd NS in 1.0 M KOH solution (a) and 1.0 M KOH + 50 mM glucose solution (b). CV curves of Pd NS during 100 potential cycle tests in 1.0 M KOH + 50 mM glucose solution (c). The scan rate is 50 mV s^{-1}.

the amperometric current increases stepwise with increasing glucose concentration up to 18 mM, and the current reaches steady-state within 9 s. The wide linear range of 0–18 mM completely covers the normal physiological level of glucose (3–8 mM) in human blood. As depicted in Figure 6(a), the calibration plot of current density versus glucose concentration illustrates the regression equation of j (mA cm^{-2}) = 0.202 + 0.032 c (mM) with a correlation coefficient (R^2) of 0.999, which exhibits a sensitivity of 32 μA mM^{-1} cm^{-2}. The detection limit is further calculated to be 2.0 μM based on the signal to noise ($S/N = 3$). Table II compares the sensitivity, linear range and detection limit between Pd NS and other developed Pd nanostructured electrodes used for non-enzymatic glucose sensing. The sensitivity of Pd NS electrode is higher than that of the literatures for nanoporous PdNi [16], nanoporous PdCu [24] and Pd nanoparticles supported on functional carbon nanotubes [52]. The superior electrochemical properties of Pd NS electrode in monitoring glucose can be attributed to the bicontinous nanostructure with larger pore size, which increases the activity surface and accelerates the electron-transfer reaction. Here it is the existing of Cu in the top surface of Pd NS which produces synergistic effect with Pd that is another reason of the high electrochemical activity of the as-prepared Pd NS electrode. The higher sensitivity, wide linear range and low detection limit obtained on the Pd NS are very attractive.

Selectivity is one of important properties of glucose sensors in the detection of human blood, which contains several possible interfering substances, such as ascorbic acid (AA) and uric acid (UA). Considering that the normal physiological level of glucose is more than 10 times higher than those of interfering species (<0.5 mM), the interference test was performed by the successive addition of 1 mM glucose, 0.1 mM AA and 0.1 mM UA into 0.1 M KOH. As demonstrated in Figure 6(b), upon successive addition of glucose, AA and UA, it is found that the amperometric response of the Pd NS electrode to AA is less than 8% of that to glucose and almost no current response for UA, implying that the Pd NS electrode has high selectivity and can be employed to detect glucose with negligible interference from AA and UA. Figure 6(c) displays the CV curves of the Pd NS electrode in 1.0 M KOH in the presence of 50 mM glucose at different scan rates (10–100, 125, 150, 175, 200, 250, 300 mV s^{-1}). The anodic peak shows a significantly positive shift, the cathodic peak shifts negatively and the redox peak current densities increase with the increasing of the potential scan rate, indicating a rapid and reversible redox reaction. Moreover, Figure 6(d) reveals that there exists a linear relationship between both the redox peak current densities and the square root of potential scan rates ($v^{1/2}$), suggesting that the electrochemical kinetics is a typical diffusion-controlled electrochemical process [27], which is ideal for glucose sensing.

3.3. Discussion

As above-mentioned results, a Pd nanosponge architecture is formed on the Ti–Zr–Cu–Pd amorphous alloy under the

Table I. Summary of the onset potential, peak potential, peak current density of Pd plate and Pd NS in the forward and backward scan in CV measurements conducted in 1.0 M KOH + 50 mM glucose solution.

		Peak potential (V)		Peak current density, mA cm^{-2}		
Sample	E_{onset} (V)	Forward scan	Backward scan	Forward scan	Backward scan	Peak ratio, j_F/j_B
Pd plate	−0.40	−0.26	−0.41	3.1	2.6	1.2
Pd NS	−0.49	−0.20	−0.41	14.0	−6.1	2.3

electrochemical treatment with current density of 10 mA cm^{-2}. The potential differences between Pd and Ti, Pd and Zr, Pd and Cu are 2.545 V, 2.444 V and 0.573 V, respectively. The large differences of standard electrode potential between the elements will support Ti, Zr and Cu, which have high chemical activity, to be dissolved preferentially before Pd [28]. In F^- containing solution, the main element of Ti (Zr) will be oxidized to $[TiF_6]^{2-}$ ($[ZrF_6]^{2-}$) with high solubility and the dissolution of Ti (Zr) will be accelerated under the high anodic current density.

The formation of sponge-like structure is mainly controlled by the dissolution of the less noble Ti, Cu and Zr in the $Ti_{40}Zr_{10}Cu_{36}Pd_{14}$ amorphous alloy. With the dissolution of less noble atoms Ti, Zr and Cu with standard potentials of −1.630 V, −1.529 V and 0.342 V, the Pd atoms (0.915 V) diffuse and rearrange to agglomerate into clusters. In the system of Ti–Cu, Cu will remain in the F^- containing solution [29], but in this more complex system of Ti–Zr–Cu–Pd with Pd element, the standard electrode potential difference between Cu and Pd also leads to the dissolution of Cu in the following step. As a result, an open interpenetrating nanoporous Pd structure is formed by atomic diffusion and rearrangement. At the early stage, Ti and Zr are anodic oxidized primarily and dissolved partially. Accordingly the remaining Ti containing alloy tends to form a tubular structure by self-assembly under the effects of F^- ion [30, 31]. In the subsequent dealloying stage, Cu and residual supporting skeleton of TiO_2 are further dissolved, leading to the formation of nanosponge structure with main element Pd and trace element Cu retained. Consequentially, this sponge-like structure is formed by the self-assembly process through surface diffusion [32], where the cubic Pd with grain size of several nanometers are born [33]. Here, the precursor in amorphous state is believed to be

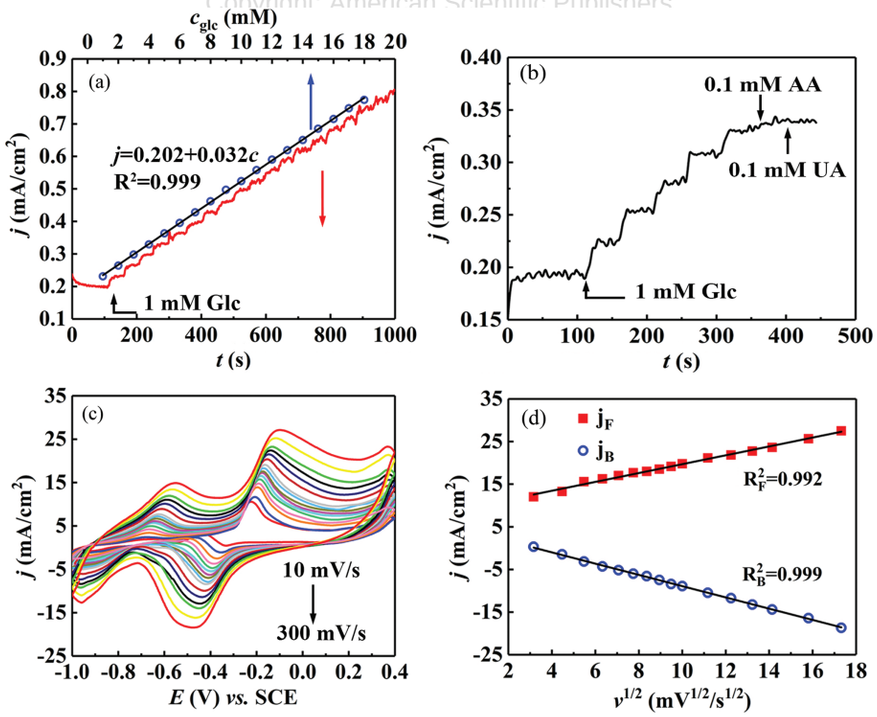

Figure 6. Amperometric current response of Pd NS on successive addition of 1 mM glucose into stirring 0.1 M KOH solution at −0.25 V and the plot of current density versus glucose concentrations (a), interference test of the Pd NS in 0.1 M KOH electrolyte with 1 mM glucose, 0.1 mM AA and 0.1 mM UA at −0.25 V (b). CV curves of glucose electro-oxidation on the Pd NS electrode in 1.0 M KOH + 50 mM glucose at different scan rates (c), and the plot of redox peak current densities versus the square root of the scan rate (d).

Table II. Comparison of the sensitivity, linear range and detection limit between Pd NS and Pd nanostructured electrodes used for non-enzymatic glucose sensing.

Electrode	Sensitivity (μA mM^{-1} cm^{-2})	Linear range (mM)	Detection limit (μM)	Refs.
NP–PdNi	0.75	1–25	1.9	[17]
Pd nanocubes	34	1–10	–	[23]
NP–PdCu	1.6	1–30	1.9	[24]
Pd–Co CNTs	3.8	0.01–2.4	1	[49]
Pd NPs	17.7	1–8	237	[50]
NP Pt	5.67	1–10	0.8	[51]
Pd/CNT	11.4	0–46	–	[52]
Pd NS	32	1–18	2.0	This work

beneficial for the formation of ultrafine Pd nanosponge during the dealloying process.

On the other hand, the synergistic catalytic effect between Pd and Cu enhances the electrocatalytic activity of Pd NS toward glucose oxidation [34, 35]. According to reported literatures [36], a Pd–Au bimetallic nanoparticle tube can remarkably enhance the catalytic activity by tuning the interface of Pd–Au. As is well known that the role of catalysts is to accelerate the electron transfer between reactants, which requires the catalyst to have both the ability to accept electrons and the ability to give electrons [37]. From the view of electron configuration, the *d*-orbital vacancies of transition metal Pd with distinctive electron configuration result in high catalytic activity [33, 38]. The formation of bimetallic Pd/Cu interface with Pd and residual Cu nanoparticle changes the electronic structure and *d*-orbital vacancies [39, 40]. On the basis of d-band center theory, a decrease of *d*-orbitals overlap between Pd and Cu atoms occurs at the interface of bimetallic Pd/Cu and narrows the *d*-band, which shifts up the *d*-band center and leads to the prominent enhancement of catalytic activity [41–44].

In addition, the superior catalytic performance of Pd NS is attributed to its ultrafine microstructure with high surface area, which plays important role in supporting more electrochemical reaction sites [14, 17, 24]. The unique sponge-like structure with hollow interior in Pd NS facilitates the effective catalyst process in both the exterior and the interior surfaces. In this special structure, both of the internal and the external surfaces of the Pd NS are accessible to the reactants and provide much more active sites which are necessary for the electro-oxidation [45]. Moreover, the unique nanoporous morphology acts as a reservoir for trapping OH^- anions which can be strongly chemisorbed onto the Pd NS surface to form surface oxygenated species [46]. Those species enhance the onset and proceeding of glucose electro-oxidation reactions and further promote the oxidation of absorbed intermediates on the Pd NS surface. The ultrafine nanoporous structures are advantageous to the oxidation of any poisonous intermediates and improve the resistance to the carbonaceous species accumulation [47], which directly accelerate the glucose electro-oxidation with a great increase in the reverse anodic peak current density. The tolerance of the catalysis to CO can be characterized by the ratio of the forward and backward anodic peak currents, j_F/j_B. Pd NS's high j_F/j_B value of ~2.3, versus 0.76 for the commercial Pt/C NP electrocatalysts [48], is an indication of its great poisoning tolerance to carbonaceous oxidative intermediates. The economical Pd electrode with high CO poisoning tolerance makes it promising candidate as a next-generation electrocatalyst, since Pt electrode suffers from limitations of its high cost and high susceptibility to poisoning by CO. Furthermore, in this research, the atom ratio of Pd to other elements in precursor alloy is only 14:86, indicating that only low Pd loading is needed to obtain such Pd NS catalyst with superior electrocatalytic activity and high stability, which further highlights the high application potential of Pd NS as an electrocatalyst.

4. CONCLUSION

Novel Pd nanosponge, with pore size of ~15.5 nm, is successfully fabricated by one-step dealloying of $Ti_{40}Zr_{10}Cu_{36}Pd_{14}$ amorphous alloy at a constant current density of 10 mA cm^{-2} in 1.0 M $(NH_4)_2SO_4$ + 0.5 wt% NH_4F solution. The onset potentials of glucose electro-oxidation for Pd NS significantly shift to the negative direction, compared with the Pd plate electrode. Moreover, the Pd NS exhibit about 4.5 times higher oxidation current for glucose electro-oxidation. The higher ratio of the forward and backward anodic peak currents (j_F/j_B, ~2.3) indicates better tolerance of the catalysis to CO on the Pd NS electrode. Enhanced catalytic activity of Pd NS is attributed to the bimetallic synergistic effect and the large active surface area of the high-uniformity nanoporous structure. The facile synthesis of the cost-effective Pd NS electrode with superior electrocatalytic performance towards glucose oxidation will open up a new avenue for the design and construction of the advanced non-Pt electrocatalysts.

Acknowledgments: This work is financially supported by the Natural Science Foundation of China (No. 51301091), the Natural Science Foundation of Jiangsu Province (BK20171424), National Defense Basic Scientific Research Program of China (JCKYO8414C020) and State Key Lab of Advanced Metals and Materials (2018-2D04).

References and Notes

1. Erlebacher, J., Aziz, M.J., Karma, A., Dimitrov, N. and Sieradzki, K., **2001**. Evolution of nanoporosity in dealloying. *Nature*, *410*(6827), pp.450–453.
2. Ding, Y. and Chen, M.W., **2009**. Nanoporous metals for catalytic and optical applications. *MRS Bulletin*, *34*(8), pp.569–576.

3. Liu, L.F., Pippel, E., Scholz, R. and GÖsele, U., **2009**. Nanoporous Pt–Co alloy nanowires: Fabrication, characterization, and electrocatalytic properties. *Nano Letters*, *9*(12), pp.4352–4358.
4. Masuda, H. and Fukuda, K.,**1995**. Ordered metal nanohole arrays made by a two-step replication of honeycomb structures of anodic alumina. *Science, 268*(5216), pp.1466–1468.
5. Thorp, J.C., Sieradzki, K., Tang, L., Crozier, P.A., Misra, A., Nastasi, M., Mitlin, D. and Picraux, S.T., **2006**. Formation of nanoporous noble metal thin films by electrochemical dealloying of $Pt_xSi_{(1-x)}$. *Applied Physics Letters, 88*(3), pp.033110–033113.
6. Singh, E. and Nalwa, H.S., eds., **2019**. *Nanomaterial-Based Flexible and Multifunctional Sensors*, Los Angeles, American Scientific Publishers.
7. Krishnan, S.K., Singh, E., Singh, P., Meyyappan, M. and Nalwa, H.S., **2019**. A review on graphene-based nanocomposites for electrochemical and fluorescent biosensors. *RSC Advances*, *9*(16), pp.8778–8881.
8. Singh, E., Meyyappan, M. and Nalwa, H.S., **2017**. Flexible graphene-based wearable gas and chemical sensors. *ACS Applied Materials & Interfaces*, *9*(40), pp.34544–34586.
9. Rugolo, J., Erlebacher, J. and Sieradzki, K., **2006**. Length scales in alloy dissolution and measurement of absolute interfacial free energy. *Nature Materials, 5*(12), pp.946–949.
10. Dan, Z.H., Qin, F.X., Wada, T., Yamaura, S., Xie, G.Q., Sugawara, Y., Muto, I., Makino, A. and Hara, N., **2013**. Nanoporous palladium fabricated from an amorphous $Pd_{42.5}Cu_{30}Ni_{7.5}P_{20}$ precursor and its ethanol electro-oxidation performance. *Electrochimica Acta*, *108*, pp.512–519.
11. Lee, G.H., An, S., Jang, S.W., Hwang, S., Lim, S.H. and Han, S., **2017**. Fabrication of nanoporous noble metal thin films by O_2 plasma dealloying. *Thin Solid Films*, *631*, pp.147–151.
12. Hakamada, M. and Mabuchi, M., **2009**. Preparation of nanoporous palladium by dealloying: Anodic polarization behaviors of Pd–M (M = Fe, Co, Ni) alloys. *Materials Transactions*, *50*(3), pp.431–435.
13. Hui, S.C., Zhang, J., Chen, X.J., Xu, H.H., Ma, D.F., Liu, Y.L. and Tao, B.R., **2011**. Study of an amperometric glucose sensor based on Pd–Ni/Si NW electrode. *Sensors and Actuators B: Chemical*, *155*(2), pp.592–597.
14. Wu, X.W., Chen, F., Huang, M., Dan, Z.H. and Qin, F.X., **2019**. Ni-decorated ZrAlCo–O nanotube arrays with ultrahigh sensitivity for non-enzymatic glucose sensing. *Electrochimica Acta*, *311*, pp.201–210.
15. Zhang, S., Chen, F., Chi, Y.C., Dan, Z.H. and Qin, F.X., **2019**. Non-enzymatic electrochemical glucose sensor based on Ti–Cu–O nanotubes prepared from TiCu amorphous alloy. *Journal of Nanoscience and Nanotechnology*, *19*(7), pp.3825–3831.
16. Zhao, D.Y. and Xu, C.X., **2015**. A nanoporous palladium-nickel alloy with high sensing performance towards hydrogen peroxide and glucose. *Journal of Colloid and Interface Science*, *447*, pp.50–57.
17. Yang, C.L., Zhang, X. H., Lan, G., Chen, L.Y., Chen, M.W., Zeng, Y.Q. and Jiang, J.Q., **2014**. Pd-based nanoporous metals for enzyme-free electrochemical glucose sensors. *Chinese Chemical Letters*, *25*(4), pp.496–500.
18. Hakamada, M. and Mabuchi, M., **2009**. Fabrication nanoporous palladium by dealloying and its thermal coarsening. *Journal of Alloys and Compounds*, *479*(1–2), pp.326–329.
19. Wang, X.G., Wang, W.M., Qi, Z., Zhao, C.C., Ji, H. and Zhang, Z.H., **2010**. Fabrication, microstructure and electrocatalytic property of novel nanoporous palladium composites. *Journal of Alloys and Compounds*, *508*(2), pp.463–470.
20. Yu, J.S., Ding, Y., Xu, C.X., Inoue, A., Sakurai, T. and Chen, M.W., **2008**. Nanoporous metals by dealloying multicomponent metallic glasses. *Chemistry of Materials*, *20*(14), pp.4548–4550.
21. Zhou, Y.Y., Niu, M.Y., Zhu, S.L., Liang, Y.Q., Cui, Z.D., Yang, X.J. and Inoue, A., **2019**. Preparation and electrocatalytic performance of nanoporous Pd/Sn and Pd/Sn–CuO composite catalysts. *Electrochimica Acta*, *296*, pp.397–406.
22. Li, R., Liu, X.J., Wang, H., Wu, Y., Chan, K.C. and Lu, Z.P., **2019**. Sandwich nanoporous framework decorated with vertical CuO nanowire arrays for electrochemical glucose sensing. *Electrochimica Acta*, *299*, pp.470–478.
23. Ye, J.S., Chen, C.W. and Lee, C.L., **2015**. Pd nanocube as non-enzymatic glucose sensor. *Sensors and Actuators B: Chemical*, *208*, pp.569–574.
24. Yang, H.X., Wang, Z.H., Li, C.C. and Xu, C.X., **2017**. Nanoporous PdCu alloy as an excellent electrochemical sensor for H_2O_2 and glucose detection. *Journal of Colloid and Interface Science*, *491*, pp.321–328.
25. Kuang, Y.J., Wu, B.H., Hu, D., Zhang, X.H. and Chen, J.H., **2012**. One-pot synthesis of highly dispersed palladium nanoparticles on acetylenic ionic liquid polymer functionalized carbon nanotubes for electrocatalytic oxidation of glucose. *Journal of Solid State Electrochemistry*, *16*(2), pp.759–766.
26. Wang, X.G., Wang, W.M., Qi, Z., Zhao, C.C., Ji, H. and Zhang, Z.H., **2010**. Electrochemical catalytic activities of nanoporous palladium rods for methanol electro-oxidation. *Journal of Power Sources*, *195*(19), pp.6740–6747.
27. Yang, Y., Wang, Y.L., Bao, X.Y. and Li, H.C., **2016**. Electrochemical deposition of Ni nanoparticles decorated ZnO hexagonal prisms as an effective platform for non-enzymatic detection of glucose. *Journal of Electroanalytical Chemistry*, *775*, pp.163–170.
28. Zhang, M., Li, M.P., Yin, T. and Zhang, T., **2016**. Fabrication of nanoporous bi-metallic Ag-Pd alloys with open pores. *Materials Letters*, *162*, pp.273–276.
29. Dan, Z.H., Qin, F.X., Makino, A., Sugawara, Y., Muto, I. and Hara, N., **2014**. Fabrication of nanoporous copper by dealloying of amorphous Ti–Cu–Ag alloys. *Journal of Alloys and Compounds*, *586*, pp.S134–S138.
30. Sopha, H., Pohl, D., Damm, C., Hromadko, L., Rellinghaus, B., Gebert, A. and Macak, J.M., **2017**. Self-organized double-wall oxide nanotube layers on glass-forming Ti–Zr–Si(–Nb) alloys. *Materials Science and Engineering C*, *70*(Pt.1), pp.258–263.
31. Parcharoen, Y., Kajitvichyanukul, P., Sirivisoot, S. and Termsuksawad, P., **2014**. Hydroxyapatite electrodeposition on anodized titanium nanotubes for orthopedic applications. *Applied Surface Science*, *311*, pp.54–61.
32. Wang, S.S. and Liu, L., **2017**. Fabrication of novel nanoporous copper powder catalyst by dealloying of ZrCuNiAl amorphous powders for the application of wastewater treatments. *Journal of Hazardous Materials*, *340*, pp.445–453.
33. Wang, S.S., Zhang, C., Li, H.Y. and Liu, L., **2017**. Enhanced electrocatalytic performance of Pd-based amorphous nanoporous structure synthesized by dealloying $Pd_{32}Ni_{48}P_{20}$ metallic glass. *Intermetallics*, *87*, pp.6–12.
34. Shih, Z.Y., Wang, C.W., Xu, G. and Chang, H.T., **2013**. Porous palladium copper nanoparticles for the electrocatalytic oxidation of methanol in direct methanol fuel cells. *Journal of Materials Chemistry A*, *1*(15), pp.4773–4778.
35. Wu, W.P., Periasamy, A.P., Lin, G.L., Shih, Z.Y. and Chang, H.T., **2015**. Palladium copper nanosponges for electrocatalytic reduction of oxygen and glucose detection. *Journal of Materials Chemistry A*, *3*(18), pp.9675–9681.
36. Cui, C.H., Yu, J.W., Li, H.H., Gao, M.R., Liang, H.W. and Yu, S.H., **2011**. Remarkable enhancement of electrocatalytic activity by tuning the interface of Pd–Au bimetallic nanoparticle tubes. *ACS Nano*, *5*(5), pp.4211–4218.
37. Zhang, R.G., Yang, M., Peng, M., Ling, L.X. and Wang, B.J., **2019**. Understanding the role of Pd: Cu ratio, surface and electronic structures in Pd–Cu alloy material applied in direct formic acid fuel cells. *Applied Surface Science*, *465*, pp.730–739.
38. Hu, Y.C., Wang, Y.Z., Su, R., Cao, C.R., Li, F., Sun, C.W., Yang, Y., Guan, P.F., Ding, D.W., Wang, Z.L. and Wang, W.H., **2016**. A highly

efficient and self-stabilizing metallic-glass catalyst for electrochemical hydrogen generation. *Advanced Materials*, *28*(46), pp.10293–10297.

39. Hammer, B. and Nørskov, J.K., **1995**. Electronic factors determining the reactivity of metal surfaces. *Surface Science*, *343*(3), pp.211–220.

40. Modwi, A., Ghanem, M.A., Al-Mayouf, A.M. and Houas, A., **2018**. Lowering energy band gap and enhancing photocatalytic properties of Cu/ZnO composite decorated by transition metals. *Journal of Molecular Structure*, *1173*, pp.1–6.

41. Kitchin, J. R., Nørskov, J.K., Barteau, M.A. and Chen, J.G., **2004**. Modification of the surface electronic and chemical properties of Pt(111) by subsurface 3*d* transition metals. *Journal of Chemical Physics*, *120*(21), pp.10240–10246.

42. Hu, S.Z., Che, F.L., Khorasani, B., Jeon M., Yoon, C.W., McEwen, J.S., Scudiero, L. and Ha, S., **2019**. Improving the electrochemical oxidation of formic acid by tuning the electronic properties of Pd-based bimetallic nanoparticles. *Applied Catalysis B: Environmental*, *254*, pp.685–692.

43. Crampton, A.S., Rötzer, M.D., Schweinberger, F.F., Yoon, B., Landman, U. and Heiz, U., **2016**. Ethylene hydrogenation on supported Ni, Pd and Pt nanoparticles: Catalyst activity, deactivation and the *d*-band model. *Journal of Catalysis*, *333*, pp.51–58.

44. Zhou, Y., Zhou, Z.Z., Shen, R.X., Ma, R.G., Liu, Q., Cao, G.Z. and Wang, J.C., **2018**. Correlating electrocatalytic oxygen reduction activity with *d*-band centers of metallic nanoparticles. *Energy Storage Materials*, *13*, pp.189–198.

45. Gao, J.J., Zhou, G.P., Qiu, H.J., Wang, Y. and Wang, J.Q., **2016**. Dealloying monolithic Pt–Cu alloy to wire-like nanoporous structure for electrocatalysis and electrochemical sensing. *Corrosion Science*, *108*, pp.194–199.

46. Haghighi, B., Karimi, B., Tavahodi, M. and Behzadneia, H., **2015**. Fabrication of a nonenzymatic glucose sensor using Pd-nanoparticles decorated ionic liquid derived fibrillated mesoporous carbon. *Materials Science and Engineering C*, *52*, pp.219–224.

47. Peng, C., Yang, W.K., Wu, E.Y., Ma, Y.Y., Zheng, Y.X., Nie, Y.T., Zhang, H. and Xu, J., **2017**. PdAg alloy nanotubes with porous walls for enhanced electrocatalytic activity towards ethanol electrooxidation in alkaline media. *Journal of Alloys and Compounds*, *698*, pp.250–258.

48. Koenigsmann, C. and Wong, S.S., **2011**. One-dimensional noble metal electrocatalysts: A promising structural paradigm for direct methanol fuel cells. *Energy & Environmental Science*, *4*, pp.1161–1176.

49. Huang, B.B., Wang, Y., Lu, Z.W., Du, H.J. and Ye, J.S., **2017**. One pot synthesis of palladium-cobalt nanoparticles over carbon nanotubes as a sensitive non-enzymatic sensor for glucose and hydrogen peroxide detection. *Sensors and Actuators B Chemical*, *252*, pp.1016–1025.

50. Wang, F.X., Niu, X.B., Wang, W., Jing, W.L., Huang, Y.L. and Zhan, J., **2018**. Green synthesis of Pd nanoparticles via extracted polysaccharide applied to glucose detection. *Journal of the Taiwan Institute of Chemical Engineers*, *93*, pp.87–93.

51. Weremfo, A., Fong, S.T.C., Khan, A., Hibbert, D.B. and Zhao, C., **2017**. Electrochemically roughened nanoporous platinum electrodes for non-enzymatic glucose sensors. *Electrochimica Acta*, *231*, pp.20–26.

52. Chen, X.M., Lin, Z.J., Chen, D.J., Jia, T.T., Cai, Z.M., Wang, X.R., Chen, X., Chen, G.N. and Oyama, M., **2010**. Nonenzymatic amperometric sensing of glucose by using palladium nanoparticles supported on functional carbon nanotubes. *Biosensors & Bioelectronics*, *25*(7), pp.1803–1808.

Received: 22 October 2019. Accepted: 30 March 2020.